Mechanisms of damage formation in Eu-implanted AlN

S. Leclerc, B. Lacroix, A Decl, K. Lorenz, P. Ruterana

Mechanisms of damage formation in Eu-implanted AlN

S. Leclerc,[1,a)] B. Lacroix,[1] A. Declémy,[2] K. Lorenz,[3] and P. Ruterana[1,a)]
[1]*CIMAP, CNRS-CEA-ENSICAEN-UCBN, 6 Bd Maréchal Juin, 14050 Caen Cedex 4, France*
[2]*Institut Pprime, Département Physique et Mécanique des Matériaux, CNRS-Université de Poitiers-ENSMA, BP 30179, 86 962 Futuroscope-Chasseneuil Cedex, France*
[3]*Instituto Tecnológico e Nuclear, Instituto Superior Técnico, Universidade Técnica de Lisboa, EN 10, 2686-953 Savacém, Portugal*

(Received 27 July 2012; accepted 12 September 2012; published online 10 October 2012)

X-ray diffraction (XRD) and transmission electron microscopy (TEM) were used to investigate the evolution of damage during implantation of 300 keV Eu ions at room temperature in AlN. At low fluence, a strain increase is observed in a buried layer where clusters of point defects and stacking faults (SFs) coexist. At higher fluence, a saturation of the strain is observed in this layer, and the XRD curves exhibit characteristic features which coupled with TEM results enable the identification of additional, spatially separated, dilated and contracted regions. From these observations, the following damage mechanisms are proposed. As the SFs grow by trapping point defects, a dense network of basal and prismatic SFs forms, which leads to the ejection of point defects from the buried damaged layer and consequently to the saturation of the strain. In this process, interstitials in excess migrate towards the undamaged bulk where they form clusters inducing large strain values. In contrast, defects ejected towards the surface either remain isolated or form isolated dislocation loops and SFs depending on their nature, i.e., interstitial or vacancy. This is probably the main difference with GaN where the defects ejected from the buried damaged layer contribute to the fast propagation of the dense SFs network towards the surface due to their relatively low formation energies. As a consequence, whilst nanocrystallization occurs at the surface of GaN, the relative confinement of defects and implanted atoms in the buried layer of AlN results in its amorphization, although at extremely high fluences ($\sim 10^{17}$ Eu/cm^2). © *2012 American Institute of Physics*. [http://dx.doi.org/10.1063/1.4758311]

I. INTRODUCTION

Today's challenges in semiconductor industry include the integration of optoelectronics into standard microelectronics, in compliance with requirements of miniaturization, low cost and mass production, as well as the production of more efficient electroluminescent devices. To face these challenges, doping of semiconductors with rare earth (RE) elements has been proposed. In particular, the nitride-based III-V semiconductors with large band gaps have been investigated as promising host matrices for these elements.[1–3] Among them, AlN has the highest thermal conductivity, the largest band gap (6.2 eV), which should ensure a low quenching of luminescence,[4,5] and strong potential for light emitters and detectors. For most applications, the doping process requires the introduction of rare earth atoms above the solid solubility limit with a good control of the concentration profile and the compatibility with conventional industrial technologies. These requirements are fulfilled by ion implantation that however generates defects along the ion paths which are detrimental to the structural and physical properties of the implanted material. In particular, dislocations and stacking faults are known to have adverse effects on optoelectronic properties of semiconducting materials.[6] A complete understanding of the damage mechanisms acting during implantation is thus necessary towards the design and manufacturing of high-performance and reliable devices. While many reports have already been published on the study of the microstructural modifications induced by ion implantation[7–10] and more specifically RE ion implantation[11–15] into GaN, few were dedicated to AlN.[16–19] These few works were mainly based on RBS/C and TEM experiments that are, respectively, sensitive to the lattice disorder and the extended defects. To obtain new insights into the understanding of the damage generated during ion implantation in AlN, we have taken advantage of the high sensitivity of the XRD technique to the lattice strain. As the strain mainly results from the defects generated by ion implantation, mechanisms such as recombination of defects and migration of interstitials have for example been detected in SiC,[20] thanks to XRD. In the present study, XRD experiments performed on Eu-implanted AlN are complemented with TEM experiments and compared to previous RBS/C measurements.[19] The results are here discussed in the light of those recently reported in GaN using similar procedures and conditions of implantation.[21]

II. EXPERIMENTAL DETAILS

Thick (0001) AlN films ($\sim 3\ \mu$m) from Technologies and Devices International Inc. grown by hybride vapor phase epitaxy on (0001) sapphire substrates were implanted at room temperature (RT) with 300 keV Eu ions to fluences ranging from 1×10^{13} to 1×10^{17} cm^{-2}. Both channeled implantations along the c-axis and random implantations with the

a)Authors to whom correspondence should be addressed. Electronic addresses: stephanie.jublot-leclerc@csnsm.in2p3.fr and ruterana@ensicaen.fr.

surface normal 10° off the beam direction were performed. Calculations using SRIM code[22] give the mean projected range of ions, R_P, at about 80 nm and the peak of damage (vacancies), R_D, around 55 nm for the random configuration. Such calculations predict that the surface damaged layer is contained within the first 100 nm. The implanted samples were studied using x-ray diffraction (XRD) and transmission electron microscopy (TEM). XRD measurements were conducted in the Bragg (reflection) geometry on an automated laboratory-made two circles goniometer with the radiation $K_{\alpha 1}$ of copper ($\lambda = 1.5405$ Å) provided by a 5 kW RIGAKU RU-200 generator with a vertical linear focus in combination with a quartz monochromator.[23] θ-2θ scans were carried out near the (0002) Bragg reflection ($2\theta_B = 36.02°$) using 0.005° stepping motors. For this reflection, the penetration depth of x-rays is significantly larger than the implanted layer which enables relative measurements of the strain by comparing the surface implanted layer to the underlying unperturbed bulk. According to the derivation of the Bragg's law, the strain along the surface normal, ε_N, is directly determined by plotting the θ-2θ curves against $q_{[0001]}/H_{(0002)}$, where $q_{[0001]}$ is the deviation from the reciprocal lattice vector $H_{(0002)}$ of the (0002) planes in the direction of the sample surface. In addition to strain, XRD curves carry information of disorder (clustering of defects, amorphization, etc.) via the static Debye-Waller factor Wh that weights the scattered intensity.[24–26] Cross-sections for TEM were thinned down to less than 10 μm by mechanical polishing, and then argon ion milled at low energy and LN_2 temperature in a Gatan PIPS. The TEM experiments were carried out in a JEOL 2010 F instrument operating at 200 kV. Both random and channeled implantations induce similar evolutions of strain and damage as a function of fluence as well as similar damaged structures as observed by TEM. In the following, only results obtained in the channeled geometry will be presented, but the discussion applies to both geometries.

III. RESULTS

In Fig. 1 are displayed XRD curves obtained after Eu-implantation to different fluences in AlN. All curves exhibit a main sharp Bragg peak at $q_{[0001]}/H_{(0002)} = 0$ resulting from the unperturbed bulk AlN diffraction and additional scattered intensity on the left of the main Bragg peak which is indicative of a dilatation of the lattice along the surface normal direction (for the non-implanted sample, not shown here, only the unperturbed bulk contribution is observed). At the fluence of 1×10^{13} cm^{-2}, a single satellite peak is observed at $\varepsilon_N = 0.38\%$. With increasing fluence, this satellite peak shifts towards higher values of strain up to $\varepsilon_N = 0.8\%$ at the fluence of 4×10^{14} cm^{-2}. Such curves with a single and well-defined peak can be simulated using a Gaussian-like strain profile in accordance with the defect profiles calculated with programs such as SRIM. Above 4×10^{14} cm^{-2}, the x-ray scattered intensity distribution is modified. Indeed, at the fluence of 5×10^{14} cm^{-2}, the satellite peak on the left of the Bragg peak shifts down to $\varepsilon_N = 0.7\%$ indicating a relaxation of strain (see arrow in Fig. 1), and scattered intensity appears on the right of the Bragg peak as a result of the

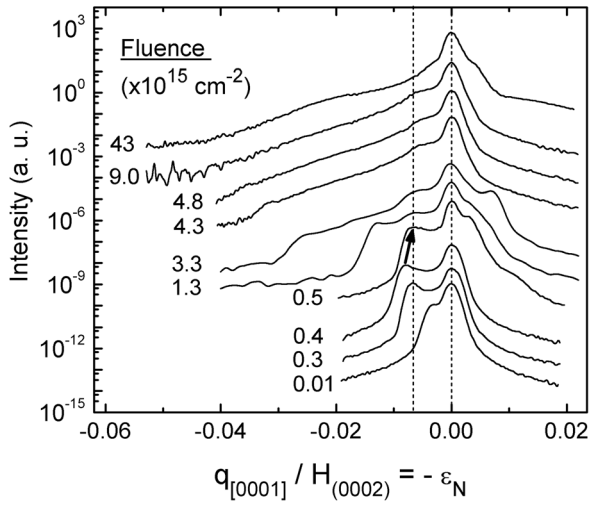

FIG. 1. X-ray scattered intensity distribution around the (0002) reflection of AlN implanted with 300 keV Eu ions at RT to different fluences. The arrow indicates a relaxation of strain.

contraction of the lattice in another region. At higher fluence, the distribution of intensity is broadened: it extends on the left of the Bragg peak from the satellite peak at 0.7%, which remains unchanged as the fluence increases (see dotted line in Fig. 1), to a maximum positive strain that increases with fluence. In parallel, the scattered intensity on the right of the Bragg peak shifts towards higher contraction values up to 3.3×10^{15} cm^{-2} and disappears at higher fluence. At 9×10^{15} cm^{-2}, the scattered intensity decreases from the peak at 0.7% down to the background level at a strain value around $\varepsilon_N = 5\%$. From this fluence, the maximum strain can no longer be determined. Above 9×10^{15} cm^{-2}, the satellite peak at 0.7% has disappeared.

The evolution of strain is plotted in Fig. 2 as a function of fluence (Fig. 2(a)) along with the damage level at the maximum of the damage profile (Fig. 2(b)) as measured from a previous RBS/C study.[19] The maximum strain values and values

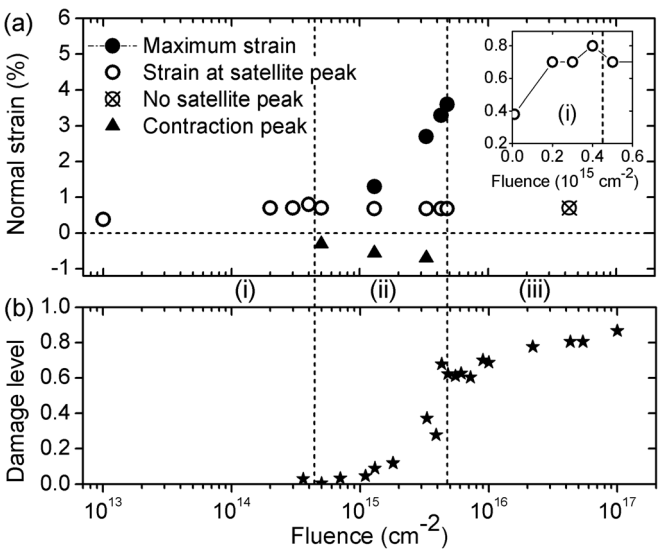

FIG. 2. Evolutions as a function of fluence of the normal strain determined from XRD measurements (a) and damage level taken as the maximum of the damage distribution measured by RBS/C[19] (b). (inset) Evolution of strain at satellite peak as a function of fluence plotted on a linear scale.

of strain at the satellite peak (positive ε_N) as well as on the right-hand side of the Bragg peak, i.e., contraction values (negative ε_N), are indicated. The values for the contraction are rough estimates as they are difficult to extract from the large peaks and shoulders observed on XRD curves. As can be noticed in the figure, whilst RBS/C results exhibit a single damage peak, XRD distinguishes three regions of different strain states. Second, at fluences lower than $1 \times 10^{15}\,\mathrm{cm}^{-2}$, RBS/C appears to be insensitive to the damage: the measured damage levels are very low (<0.05). XRD however measures non negligible strain values (which indicate the presence of defects in relatively large concentration) and points out an increase of the strain at the satellite peak (up to 0.8%) as the fluence increases up to $4 \times 10^{14}\,\mathrm{cm}^{-2}$ which is referred to as the regime (i) in Fig. 2. The next regime (ii) begins at the fluence of $5 \times 10^{14}\,\mathrm{cm}^{-2}$ with the relaxation of strain at the satellite peak which drops from 0.8 to 0.7% and the appearance of a negative strain. From then on, a positive strain from a distinct region appears to take place, and as the fluence increases in this regime, the strain at the satellite peak saturates whilst both positive and negative strains increase reaching large values. At the same time, the damage level as measured by RBS/C first increases slowly up to $1–2 \times 10^{15}\,\mathrm{cm}^{-2}$ and then more rapidly. In the last regime (iii), above $5 \times 10^{15}\,\mathrm{cm}^{-2}$, the damage level increases slowly towards unity. The maximum strain can no longer be accurately determined, and few XRD data are available. It is however important to note that the satellite peak at 0.7% has disappeared at the fluence of $4.3 \times 10^{16}\,\mathrm{cm}^{-2}$ which implies a change in the damage mechanism.

Figure 3 shows TEM micrographs of a sample implanted in channeled configuration at $3.3 \times 10^{15}\,\mathrm{cm}^{-2}$ for which a contraction peak is observed on the XRD curve. In Fig. 3(a), a dark field micrograph taken using $\mathbf{g} = 0002$ in weak beam (WB) conditions shows a buried defective layer containing clusters of point defects (white dots). The Figure 3(b) shows a less extended buried layer of planar defects visible as white horizontal segments under $\mathbf{g} = 1\bar{1}00$ WB conditions. The comparison of micrographs taken with $\mathbf{g} = 0002$ and $\mathbf{g} = 1\bar{1}00$ shows that the damaged region consists of three layers: (1) a surface layer (denoted by A on Fig. 3), 40 nm thick, where few defects are observed, (2) a buried layer of 160 nm (B on Fig. 3) where both clusters of point defects and planar defects are observed in high concentration, and (3) in the rear part, a layer of ~80 nm in width, free of planar defects but containing clusters of point defects (C on Fig. 3). As observed in HRTEM at the vicinity of the A/B interface (Fig. 3(c)), the A layer contains isolated extended defects whereas planar defects are observed in the B layer that are mainly basal stacking faults (BSFs). These BSFs are connected with prismatic stacking faults (PSFs) in much less concentration.[27] In the C layer, a gradient of contrast is observed meaning that the density of clusters decreases towards the bulk. With increasing fluence, the B layer shows longer and less frequent BSFs but does not evolve in width whilst the C layer extends deeper towards bulk (not shown here). In random configuration, this extension is largely responsible for the increase of the whole damaged layer from ~130 nm to more than 200 nm in width when the fluence increases from 1.4×10^{15} to $1 \times 10^{17}\,\mathrm{cm}^{-2}$ (see Fig. 4 in Ref. 19). At this last fluence, an amorphous layer has formed in place of the B layer: the amorphous layer (or the B layer at lower fluences) ends at a depth of about 100 nm where the C layer begins. This depth corresponds roughly to the end of the damaged layer as predicted by SRIM.

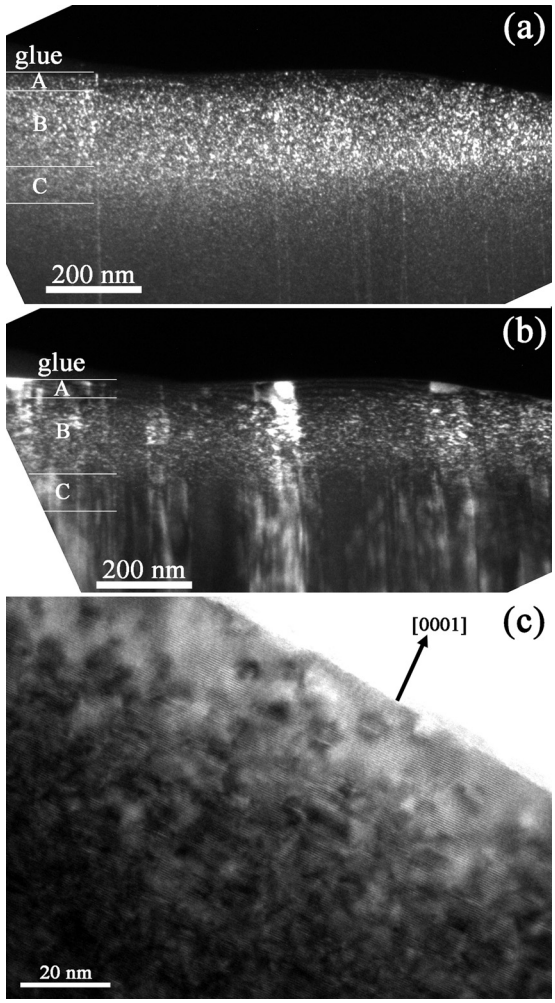

FIG. 3. Cross-sectional TEM observations of AlN after Eu implantation at $3.3 \times 10^{15}\,\mathrm{cm}^{-2}$. (a) Dark field using the $\mathbf{g} = 0002$ reflection in weak beam conditions. (b) Dark field using the $\mathbf{g} = 1\bar{1}00$ reflection in weak beam conditions. (c) HRTEM (low magnification) acquired along $[11\bar{2}0]$ close to the surface.

IV. DISCUSSION

A. Microstructural origin of strain

The whole damaged layer extends much deeper in the bulk than predicted by SRIM for random configuration. The gradient of concentration of defects in the C layer and the large increase in width of this layer with increasing fluence suggest a migration of defects from the B layer towards the undamaged bulk. We have already reported a similar occurrence in Eu-implanted GaN where the same three-layer structure was observed by TEM,[21] i.e., a surface layer that is the least damaged at low fluence, a layer with both SFs and clusters of point defects, and a layer containing solely clusters of point defects. The XRD curves of Eu-implanted AlN are also similar to those we previously reported for Eu-implanted GaN. Especially, the presence of a satellite peak

whose position remains unchanged over a wide range of fluence ($\varepsilon_N = 0.6\%$) was reported. Such peak indicates a saturation of strain in a localized layer of the implanted region. From this saturation, and similarly to the results of AlN, the scattered intensity distribution is broadened from the satellite peak to a peak at a maximum strain that increases with fluence. In GaN, the C layer containing clusters appears after the saturation of the satellite peak and evolves in width with increasing fluence as it does in AlN. Accordingly, the large tail of scattered intensity including the peak at maximum strain was attributed to the C layer and hence has to be attributed to the C layer in AlN. Moreover, the satellite peak at saturation in GaN remains after the nanocrystallization of the near surface region (layer A) that in principle impedes the diffraction of x-rays. Thus, the satellite peak in GaN, and in AlN in the present study, results from the diffraction of the B layer. This is consistent with the commonly admitted fact that stacking faults relax strains,[28–30] here in a region where the predicted concentration of defects is maximal as calculated by SRIM for the random configuration and measured by RBS/C. In the C layer, strain values larger than that in the B layer are measured as the strain induced by the large clusters is not counteracted by the formation of SFs. Therefore, the maximum strain is reached in the region where the concentration of clusters is maximal and the density of SFs minimal, i.e., in the C layer, close to the interface with the B layer.

B. Damaging processes

Previous RBS/C measurements performed by Lorenz *et al.*[19] suggest that Eu is nearly absent from the C layer of clusters. Thus, the clusters must be mainly of interstitial-type to induce the measured large positive strains. According to the SRIM code, interstitials should form approximately where the B layer of SFs forms in random implanted samples (see Fig. 4(b) in Ref. 19). Yet, the migration of interstitials during implantation induces a high concentration of clusters in the B layer as well as in the C layer. In the C layer, the combination of a high concentration of interstitials and large strain values does not induce the formation of SFs. Therefore, the SFs are not formed by a simple process of relaxation of strain by the clustering of interstitials. In contrast to the clusters, the SFs form in a layer whose width scarcely evolves with the fluence. According to SRIM calculations, this layer corresponds to the region where the maximum of energy is deposited through collision cascades. Therefore, small SFs and/or precursors like dislocation loops may form during the collision cascade process possibly by the overlapping of the dense cascades due to the high density of energy deposited by the heavy ions. In the B layer, further defects provided during implantation may either recombine, form clusters or be trapped by SFs that so grow in length. This would explain our present observations and those of Kucheyev *et al.*[31] in GaN where the average size of SFs is larger than the lateral size of cascades, meaning that SFs may not be formed in a single cascade but should instead result from a cumulative effect as their size increases with the fluence.

The defects which do not form SFs or large clusters in the cascades and which are not trapped for the growth of SFs are available for diffusion. With increasing fluence, as the network of SFs gets denser creating preferential diffusion paths for point defects, interstitials and vacancies in excess in the B layer migrate through the SFs network towards the bulk and the surface and are ejected from the B layer. Once ejected in the bulk (C layer), the interstitials obviously migrate easily being, at first, not trapped. They are indeed believed to be mobile at temperatures lower than RT in irradiated AlN.[18,32] In the B layer, this flow out and more generally the interaction of point defects with SFs (including recombination and trapping of point defects) induce a relaxation of strain followed by a saturation of strain (see arrow and dotted line in Fig. 1) whilst the SFs continue to grow as observed by TEM and the RBS/C peak damage[19] still increases. In the C layer, migrating interstitials can agglomerate and form clusters that grow and become large inducing a low static Debye-Waller factor Wh, and hence, a low scattered intensity as observed at high strain values on XRD curves (see Fig. 1). Finally, the migration of interstitial-type defects is probably hindered in the C layer as the clusters become numerous and large increasing the probability of interaction between the defects and clusters. As the lowest Wh is obtained at the highest strain values, this means most probably that the interface between the B and C layer contains the largest clusters which act as traps for the interstitials ejected from the B layer. As a consequence, further migration of interstitials towards the undamaged bulk is inhibited leading to a frozen distribution of clusters in the C layer. The direct effect is that the distribution of x-ray scattered intensity does not change any more at high fluence. As seen in Fig. 1, the XRD curves are indeed very similar between 4.8 and $9 \times 10^{15}\,\mathrm{cm}^{-2}$ except at high strain values where the low Wh leads to scattered intensities lower than the background level. This impedes the observation of the evolution of the strain at the B-C interface (maximum strain) where interstitials and clusters are likely to accumulate at high fluence.

C. Specificities of AlN with respect to GaN

The above processes are common to AlN and GaN implanted in the same conditions as shown by similar XRD results and three-layer damage structures. Both nitrides thus appear to have similar damaging processes. However, in GaN, the ejection of defects out of the B layer not only accelerates the damaging in layer C but also in layer A, which is visible on RBS/C spectra by the formation and strong evolution of a surface damage peak.[14] In this instance, the supply of defects from the B layer induces the formation of a dense SFs network at the surface, via enlargement of small SFs and SFs precursors, that eventually leads to nanocrystallization above $\sim 2 \times 10^{15}\,\mathrm{cm}^{-2}$.[21]

From our TEM and XRD results, the following specificities of AlN with respect to GaN can be noticed: (i) a contraction peak is observed at medium fluence on XRD curves (positive q/H values), (ii) the network of SFs does not reach the surface which, therefore, does not nanocrystallize. This is in agreement with the observation by RBS/C of a single

damage peak in the bulk and low damage levels close to the surface[19] whilst a bimodal evolution of damage is observed for GaN with a surface damage peak that grows higher than the bulk damage peak in concomitance with the surface nanocrystallization,[14,21] (iii) amorphization occurs at very high fluence in the B layer resulting in the disappearance of the satellite peak on XRD curves.

The contraction peak is observed on XRD curves of AlN samples implanted in both random and channeled configurations. It theoretically results from a layer containing an excess of vacancy-type defects which has to be spatially separated from the dilated regions, B and C layers, to be observed by XRD. It thus probably results from an excess of vacancies located in the near surface region. Such an excess of vacancies close to the surface can be the consequence of the spatial separation of interstitials and vacancies in the collision cascades, the effect of which should be more pronounced with increasing fluence. The channeled and random configurations lead to different distributions of damage as measured from RBS/C (not shown here) and thus probably to different distributions of point defects. Therefore, these two configurations should induce different separations between the region of excess vacancies and the region of excess interstitials.[33] However, they lead to similar contraction peaks (comparison of samples having similar maximum strain values) characterized by large contraction values and high scattered intensities. Thus, in addition to the spatial separation of vacancies and interstitials in the collision cascades, another mechanism should contribute to the contraction of the lattice in the near surface region. As shown in Fig. 2 in regime (ii), the contraction peak appears at the same time as the relaxation of strain in the B layer as the result of the ejection of defects from this layer. From then on, the contraction value increases with the fluence as does the strain value in C layer (including maximum strain). The excess of vacancies inducing the contraction peak is thus probably enhanced by the ejection of defects from the B layer. However, both vacancies and interstitials are likely to migrate from the B layer towards the surface. Therefore, interstitials reaching the A layer probably condense into defects that relax strain, i.e., dislocation loops or SFs, thus enhancing the contraction induced by isolated vacancies. As suggested by our TEM observations and underlined by Wang *et al.*,[34] BSFs observed in GaN and AlN result from the preferential condensation of interstitials on the basal planes (insertion of an extra plane). On the other hand, Wang *et al.* suggest that vacancies preferentially condense on pyramidal planes leading to the formation of PSFs. In AlN, the PSFs have formation energies that are higher than those of the BSFs of type I which are the main BSFs encountered in our samples (Table I). This is in agreement with the observation of PSFs in much less concentration than BSFs in the B layer of AlN. Interstitials can thus form BSFs in the A layer whilst vacancies in excess stay isolated inducing a contraction of the lattice.

A Fourier-filtered (0002) HRTEM analysis performed on the first tens of nanometers of the damaged surface of the sample implanted at $3.3 \times 10^{15}\,\mathrm{cm}^{-2}$ has revealed the presence of typical defects that can account for the observed

TABLE I. Stacking faults formation energies per unit cell area (in MeV/Å^2).

		AlN	GaN	Reference
BSF	Type I	49	10	35
		54	10	36
	Type II	77	20	37
		104	25	37
		103	24	35
		109	22	36
	Extrinsic	150	38	35
		164	34	36
PSF	Drum	100	22	38
	Amelinckx	100	78	38

effect (see Fig. 4). The defect labeled (1) shows the presence of one additional (0002) plane and it corresponds to a partial dislocation that bounds a large BSF. No such vacancy SFs or PSFs are observed, but some vacancy dislocation loops (defect (2)) are disseminated in the A layer. They are characterized by a local collapse of one (0002) plane resulting from the condensation of vacancies. In this image, it is also worth noticing the faulting observed in inclined lattice planes (defect (3)), which could be the next step of the vacancy clustering mechanism.[34] The disappearance at high fluence of the contraction peak on XRD curves (Fig. 1) can thus be explained by the collapse of vacancies and vacancy dislocation loops into PSFs in agreement with the observation by HRTEM of a few PSFs in the A layer of samples implanted at high fluence.[27]

In GaN, the formation energies of both BSFs and PSFs are comparable and low. Therefore, the defects which are supplied to the surface by the B layer of SFs and those produced in the cascades close to the surface are able to contribute to the formation of a SFs network which completely relaxes the strain (no contraction peak). Indeed, BSFs and PSFs form in similar concentrations in GaN whilst PSFs are found in much less concentration than BSFs in the B layer of

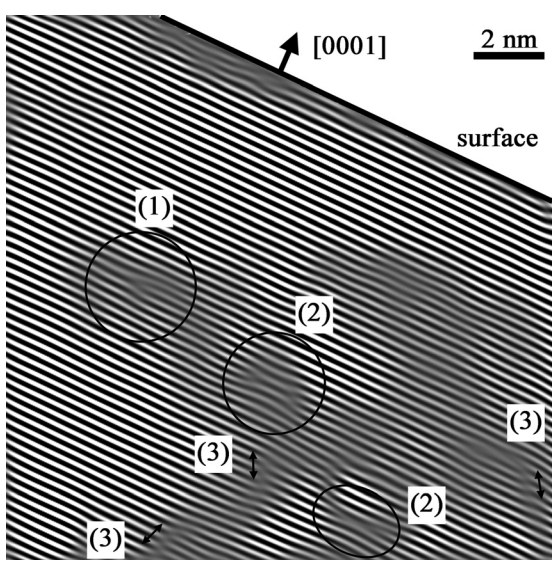

FIG. 4. Fourier-filtered (0002) HRTEM image ([11$\bar{2}$0] zone axis) of the surface of AlN after Eu implantation at $3.3 \times 10^{15}\,\mathrm{cm}^{-2}$.

AlN. Thus, the lack of connections in the SFs network (through PSFs) of AlN may hinder the migration and ejection of defects from the B layer. The absence of nanocrystallization of the surface of implanted AlN can thus be explained, in contrast to GaN, by the combination of the relative difficulty to form PSFs and the resulting hindered migration of defects. This also probably leads to the amorphization of the material as most of the defects and implanted ions are confined in the B layer. Therefore, despite similar defect processes in AlN and GaN, the difference of formation energies of SFs, especially PSFs (Table I), leads to strongly diverging evolution in their microstructures at high implantation fluence.

V. CONCLUSION

Damage induced by 300 keV Eu implantation at RT into thick (0001) AlN films was investigated using XRD and TEM. At low fluence, a single satellite peak is observed by XRD and related to a buried layer located in a region where interstitials are in excess. This layer contains both clusters of point defects and SFs which partially relax the strain induced by interstitials. It is inferred that the large SFs are formed from precursors generated in the dense cascades that grow with fluence by trapping migrating point defects. With increasing fluence, the strain increases in this layer with the increase of defects concentration up to a strain saturation at 0.7%. From this saturation, the formation of two spatially separated strained layers in contraction and in dilatation on each side of the buried layer is evidenced. To explain our observations, the following scenario is proposed. Whilst SFs continue to grow by trapping point defects, defects are ejected from the strain-saturated layer of SFs towards the surface and the bulk where they form clusters and generate large strains. Similar processes have already been reported in Eu-implanted GaN where the same three-layer structure was observed by TEM along with a similar strain distribution. However, whilst the mechanisms of damage generation are identical in both nitrides, they do not lead to the same final microstructural state at high fluence which is largely due to the lower capacity of AlN to form SFs and more particularly PSFs. The lower density of SFs and especially PSFs in AlN appears to hinder the migration of point defects as compared to GaN. Moreover, defects generated in, or reaching, the near surface layer of AlN either remain isolated or form isolated clusters and SFs in contrast to the dense network of SFs in GaN. The relative difficulty to form SFs in AlN thus impedes the surface nanocrystallization as observed in GaN.

This work has been supported by "La Région Basse-Normandie."

[1]A. J. Steckl and J. M. Zavada, MRS Bull. **24**, 9 (1999).
[2]J. M. Zavada and D. Zhang, Solid-State Electron. **38**, 1285 (1995).
[3]S. J. Pearton, J. C. Zolper, R. J. Shul, and F. Ren, J. Appl. Phys. **86**, 1 (1999) and references therein.
[4]U. Hömmerich, E. E. Nyein, D. S. Lee, A. J. Steckl, and J. M. Zavada, Appl. Phys. Lett. **83**, 4556 (2003).
[5]J. M. Zavada, N. Nepal, J. Y. Lin, H. X. Jiang, E. Brown, U. Hömmerich, J. Hite, G. T. Thaler, C. R. Abernathy, S. J. Pearton, and R. Gwilliam, Appl. Phys. Lett. **89**, 152107 (2006).
[6]F. A. Ponce and D. P. Bour, Nature (London) **386**, 351 (1997).
[7]C. Ronning, E. P. Carlson, and R. F. Davis, Phys. Rep. **351**, 349 (2001) and references therein.
[8]S. O. Kucheyev, J. S. Williams, C. Jagadish, J. Zou, and G. Li, Phys. Rev. B **62**, 7510 (2000).
[9]S. O. Kucheyev, J. S. Williams, and S. J. Pearton, Mater. Sci. Eng. R **33**, 51 (2001) and references therein.
[10]S. O. Kucheyev, J. S. Williams, C. Jagadish, J. Zou, G. Li, and A. I. Titov, Phys. Rev. B **64**, 035202 (2001).
[11]M. Mamor, V. Matias, A. Vantomme, A. Colder, P. Marie, and P. Ruterana, Appl. Phys. Lett. **85**, 2244 (2004).
[12]B. Pipeleers, S. M. Hogg, and A. Vantomme, J. Appl. Phys. **98**, 123504 (2005).
[13]F. Gloux, T. Wojtowicz, P. Ruterana, K. Lorenz, and E. Alves, J. Appl. Phys. **100**, 073520 (2006).
[14]K. Lorenz, N. P. Barras, E. Alves, I. S. Roqan, E. Nogales, R. W. Martin, K. P. O'Donnell, F. Gloux, and P. Ruterana, J. Phys. D: Appl. Phys. **42**, 165103 (2009).
[15]P. Ruterana, B. Lacroix, and K. Lorenz, J. Appl. Phys. **109**, 013506 (2011).
[16]S. O. Kucheyev, J. S. Williams, J. Zou, C. Jagadish, M. Pophristic, S. Guo, I. T. Ferguson, and M. O. Manasreh, J. Appl. Phys. **92**, 3554 (2002).
[17]E. Wendler and W. Wesch, Nucl. Instrum. Methods Phys. Res. B **242**, 562 (2006).
[18]W. Jiang, I.-T. Bae, and W. J. Weber, J. Phys.: Condens. Matter **19**, 356207 (2007).
[19]K. Lorenz, E. Alves, F. Gloux, P. Ruterana, M. Peres, A. J. Neves, and T. Monteiro, J. Appl. Phys. **107**, 023525 (2010).
[20]S. Leclerc, M. F. Beaufort, A. Declémy, and J. F. Barbot, J. Nucl. Mater. **397**, 132 (2010).
[21]B. Lacroix, S. Leclerc, A. Declémy, K. Lorenz, E. Alves, and P. Ruterana, Europhys. Lett. **96**, 46002 (2011).
[22]J. F. Ziegler and J. P. Biersack, SRIM-2003.06 computer code, see http://www.srim.org.
[23]S. Leclerc, A. Declémy, M. F. Beaufort, C. Tromas, and J. F. Barbot, J. Appl. Phys. **98**, 113506 (2005).
[24]P. H. Dederichs, Phys. Rev. B **1**, 1306 (1970). In the present publication, the static Debye-Waller factor is defined as $\exp(-L_h)$ in Dederichs notation.
[25]R. Balboni, S. Milita, and M. Servidori, Phys. Status Solidi A **148**, 95 (1995).
[26]S. Leclerc, M. F. Beaufort, J. F. Barbot, and A. Declémy, Europhys. Lett. **98**, 46001 (2012).
[27]F. Gloux, Ph.D. dissertation, Université de Caen Basse-Normandie, France, 2008.
[28]Z. H. Wu, T. Tanikawa, T. Murase, Y.-Y. Fang, C. Q. Chen, Y. Honda, M. Yamaguchi, H. Amano, and N. Sawaki, Appl. Phys. Lett. **98**, 051902 (2011).
[29]M. Gunji, A. F. Marshall, and P. C. McIntyre, J. Appl. Phys. **109**, 014324 (2011).
[30]M.-I. Richard, A. Malachias, J.-L. Rouvière, T.-S. Yoon, E. Holmström, Y.-H. Xie, V. Favre-Nicollin, V. Holý, K. Nordlund, G. Renaud, and T.-H. Metzger, Phys. Rev. B **84**, 075314 (2011).
[31]S. O. Kucheyev, J. S. Williams, and C. Jagadish, Vacuum **73**, 93 (2004).
[32]S. J. Zinkle, L. L. Snead, W. S. Eatherly, J. W. Jones, and D. K. Hensley, Mater. Res. Soc. Symp. Proc. **540**, 305 (1998).
[33]P. Levêque, H. K. Nielsen, P. Pellegrino, A. Hallén, B. G. Svensson, A. Yu. Kuznetsov, J. Wong-Leung, C. Jagadish, and V. Privitera, J. Appl. Phys. **93**, 871 (2003).
[34]C. M. Wang, W. Jiang, W. J. Weber, and L. E. Thomas, J. Mater. Res. **17**, 2945 (2002).
[35]C. Stampfl and C. G. Van de Walle, Phys. Rev. B **57**, R15052 (1998).
[36]A. F. Wright, J. Appl. Phys. **82**, 5259 (1997).
[37]J. A. Chisholm and P. D. Bristowe, J. Phys.: Condens. Matter **11**, 5057 (1999).
[38]P. Ruterana, B. Barbaray, A. Béré, P. Vermaut, A. Hairie, E. Paumier, G. Nouet, A. Salvador, A. Botchkarev, and H. Morkoç, Phys. Rev. B **59**, 15917 (1999).